

# The coordination dependence of electric-field gradients and hyperfine fields at 5sp impurities on fcc metal surfaces

S. Cottenier,<sup>1,\*</sup> V. Bellini,<sup>2,†</sup> M. Çakmak,<sup>1,3</sup> F. Manghi,<sup>2</sup> and M. Rots<sup>1</sup>

<sup>1</sup>*Instituut voor Kern- en Stralingsfysica, Katholieke Universiteit Leuven, Celestijnenlaan 200 D, B-3001 Leuven, Belgium*

<sup>2</sup>*INFM-National Research Center on nanoStructures and bioSystems at Surfaces (S3)*

*and Dipartimento di Fisica, Università di Modena e Reggio Emilia, Via Campi 213/A, I-41100 Modena, Italy*

<sup>3</sup>*Department of Physics, Gazi University, Teknikokullar, TR-06500 Ankara, Turkey*

(Dated: November 6, 2018)

We present a comparison between accurate *ab initio* calculations and a high-quality experimental data set (1986-2002) of electric-field gradients and magnetic hyperfine fields of Cd at different sites on Ni, Cu, Pd and Ag surfaces. Experiments found a systematic rule to assign surface sites on (100) and (111) surfaces based on the main component of the electric-field gradient, a rule that does not work for (110) surfaces. Our calculations show that this particular rule is a manifestation of a more general underlying systematic behavior. When looked upon from this point of view, (100), (111) and (110) surfaces behave in precisely the same way. The experimentally observed parabolic coordination number dependence of the Cd magnetic hyperfine field at Ni surfaces is verified as a general trend, but we demonstrate that individual cases can significantly deviate from it. It is shown that the hyperfine fields of other 5sp impurities at Ni surfaces have their own, typical coordination number dependence. A microscopic explanation for the different dependencies is given in terms of the details of the s-DOS near the Fermi level.

PACS numbers: 68.47.De, 68.35.Fx, 68.35.Dv, 75.70.Rf, 76.80.+y, 71.20.-b

## I. INTRODUCTION

Nuclear probe techniques, such as Mössbauer spectroscopy, Perturbed Angular Correlation spectroscopy (PAC), Nuclear Magnetic Resonance (NMR) and others, have proven in the past to be versatile tools for the study of a broad set of phenomena. By simultaneously detecting both electric-field gradients (EFG) and magnetic hyperfine fields (HFF), it has been possible to obtain a finger print of the electronic and magnetic configuration near and at the probe nucleus.<sup>1,2,3,4,5,6</sup> *Ab-initio* band structure calculations have assumed an important role in supporting, improving or confuting the interpretation of experimental data. Especially for such sensitive properties as HFF's or EFG's, the availability of these parameter-free calculations with an accuracy that is comparable with the experimental error bars, has opened new possibilities. For instance, the general behavior of the HFF induced on sp- and d-impurities embedded in bulk magnetic materials, especially in Fe and Ni, has been well characterized and the calculated values compared fairly well with the experimental ones.<sup>7,8,9,10,11</sup> Similarly, the systematics of the EFG on 5sp-impurities in non-cubic metals (Zn, Cd, Sb) have been studied by experiments and calculations (Ref. 12 and references therein). Selected calculations have been performed on more exotic systems. To name a few, the HFF and EFG on a Cd impurity atom at Fe/Co<sup>13</sup> and Fe/Ag<sup>14,15</sup> interfaces have been studied, focussing on the relation between the HFF induced on the radioactive probe atom and the magnetic moment profile across the interface. Similar studies have been performed on magnetic nanoclusters embedded in Ag<sup>16</sup> and Cu<sup>17</sup> matrices. In thin layers of *fcc* Fe on a Cu substrate, HFF and EFG at the surface and interface

have been calculated.<sup>18</sup>

If, for a few host materials, the dependence of HFF or EFG on the atomic number of the impurity atom has been studied in detail, less investigated is the variation in these properties for one specific probe atom in different environments derived from the same host material. An example of such a study – motivated by the unique capability of nuclear probe techniques to follow the diffusion of single atoms – is provided by the experiments of Voigt et al.,<sup>5</sup> recently extended and completed by Potzger et al.<sup>19</sup> Those authors put a Cd atom at different low-index Ni-surfaces and at kinks and steps on those surfaces, and measured the HFF and EFG at Cd. Overlooking the now fairly complete data set, Potzger et al. conclude that the HFF at Cd depends more or less parabolically on the *number* of Ni-atoms in the first nearest neighbor shell (NN-shell) (black dots in Fig. 3), and not on the *exact position* of those Ni-neighbors (dubbed ‘symmetry independence of the HFF’ in Ref. 20). This is attributed to a gradual change in the local DOS, not further specified. One of the two main goals of the present paper is to assess the validity of this claim, to elucidate the possible physical mechanism behind it (Sec. IV 1), and to try to extend this ‘rule’ to impurity atoms other than Cd (Sec. IV 2), all this by calculating the HFF and EFG at Cd in different Ni-environments by *ab initio* methods. A second goal is to examine the generality of common guidelines for site identification of Cd on (100) and (111) metal surfaces based on EFG measurements, as were established from experiments.<sup>3,4,21</sup> We will demonstrate that these guidelines are a manifestation of a simple and general physical mechanism that is valid for *all* low-index surfaces (Sec. III). Our work follows pioneering cluster calculations by B. Lindgren et al.<sup>22,23,24,25</sup>, who investi-

gated HFF and EFG of Cd as adatom or in a terrace site at (100) and (111) Ni surfaces, and a more systematic work by Ph. Mavropoulos et al.<sup>26</sup> for probe atoms belonging to the whole 4sp series (Cu to Sr), placed on Ni and Fe (100) surfaces. Independent from our work, some of the questions that will be discussed here were studied very recently by Ph. Mavropoulos<sup>27</sup> using a different method (full-potential KKR), a different exchange-correlation functional (LDA) and not considering atomic relaxations.

## II. METHOD AND DETAILS OF THE CALCULATIONS

For the present calculations we have employed state of the art first-principles techniques, developed within the Density Functional Theory (DFT)<sup>28,29</sup>. Most of the calculations have been performed using the full-potential augmented plane wave + local orbitals (APW+lo) method as implemented in the WIEN2k package.<sup>30</sup> We have simulated the surface+impurity complexes by using the slab-supercell approach. The impurities have been put both in an adatom site and at a substitutional position in the surface layer (called the terrace site from now on) at the three low-Miller-index surfaces, which in turn were composed of repeated slabs of 5 to 7 substrate layers (up to 11 for test calculations), separated by some vacuum space. The size and shape of the cells were chosen such to avoid artificial interaction between the impurity atoms. For symmetry reasons, the impurity atoms were placed at both sides of the slabs. Test calculations showed that about 6 Å of vacuum (equivalent to about 3.5 atomic layers) is sufficient to decouple the Cd atoms at the two surfaces, and that a similar distance is needed to decouple the Ni atoms within the same plane. More details of the slabs and the vacuum are given in tables later in the paper. As exchange-correlation functional, the PBE generalized gradient approximation (GGA)<sup>31</sup> was used. A few test calculations (see later) have been performed with the local density approximation (LDA). In the APW+lo method, wave functions, charge density, and potential are expanded in spherical harmonics within nonoverlapping atomic spheres of radius  $R_{MT}$  and in plane waves in the remaining space of the unit cell.  $R_{MT}$  values of 2.2 a.u. for Ni and 2.4 a.u. for the impurity were chosen throughout. The maximum  $\ell$  for the waves inside the atomic spheres was confined to  $\ell_{max} = 10$ . For the majority of the cases, the wave functions in the interstitial region were expanded in plane waves with a cutoff of  $K_{max} = 7.0/R_{MT}^{min} = 3.18$  a.u.<sup>-1</sup> or better, while the charge density was Fourier expanded up to  $G_{max} = 16 \sqrt{\text{Ry}}$ . For a few large cells, a lower  $K_{max} = 2.73$  a.u.<sup>-1</sup> was taken, which was tested to yield still reasonable forces. For the Brillouin zone sampling, a mesh of special k points corresponding to at least a  $14 \times 14 \times 14$  mesh (104 points) for bulk fcc Ni was taken. The lattice constant of Ni used throughout the calcu-

lations is the one which minimizes the GGA bulk total energy, i.e.  $a_{Ni}^{GGA} = 3.51$  Å. For Cu, Pd and Ag, the experimental lattice constants were used.

When the perfect crystal structure is broken, as in presence of an impurity, atomic relaxations of the atoms in the vicinity of impurity appear. Such relaxations have rather long range character, and lead to a volume change of the crystal, as testified by refined lattice parameter measurements. Additionally, since they alter the nature and strength of bonds, they change local properties such as HFF and EFG as well. Atomic relaxations tend to be the larger in size the more open is the crystal structure (e.g. zincblend)<sup>32</sup>, but it has been shown in the literature to be important also in close-packed matrices for HFF's<sup>10,11</sup> and even more for EFG's<sup>33</sup>. As taking into account atomic relaxations is computationally quite expensive, we have speeded up the calculations by using a combination of methods. First, the atomic positions were relaxed using the pseudopotential plane wave VASP code<sup>34,35</sup>. The all-electron APW+lo code was then used in a second stage to further relax the atoms to their equilibrium positions (with forces less than 1 mRy/a.u.), and to calculate the hyperfine properties.

Before proceeding with the discussion of the results, it is important to assess the accuracy of our calculated HFF's or EFG's. To this end, let us look at a well-known case, Cd in bulk Ni. The experimental value is -6.9 T (4.2 K)<sup>36</sup>. Our calculation, carried out for a large  $2 \times 2 \times 2$  32-atom supercell with relaxed nearest neighbors, yields -12.0 T. The calculation included SO-coupling (in contrast to all other calculations reported in this paper), from which we could obtain the orbital and dipolar contributions to the hyperfine field. They were smaller than 0.01 T, however, as could be expected for a closed shell atom as Cd ([Kr]5s<sup>2</sup>4d<sup>10</sup>), such that the so-called Fermi contact term<sup>37</sup> is the only contribution to the HFF. The Ni-moment was put in the [111] direction, as in nature. Without relaxation, the HFF was -9.8 T. Having taken all these precautions, we must attribute the 5.1 T difference with experiment entirely to the approximations contained in GGA. This magnitude of error is similar to the 4.2 T overestimation of the HFF for Cd in Fe, and is of the same magnitude as was found for all 5<sup>th</sup> period impurities in Fe.<sup>10,11</sup> This is the state-of-the-art for the accuracy that can be obtained currently for calculated hyperfine fields. In what follows, we can therefore expect calculated hyperfine fields that are 5 T too negative if this error is independent on the coordination number, or alternatively - if the error is more random and does not depend on the coordination number - we have to put error bars of 5 T on our results. Electric-field gradients instead can be calculated with more accuracy, and we expect here an error bar better than  $(\pm 2 \cdot 10^{21} \text{ V/m}^2)$  (see for instance Ref. 38).

### III. ELECTRIC-FIELD GRADIENTS

For an efficient discussion later in this section, we first summarize a few properties and conventions with respect to the electric-field gradient (EFG) at a nucleus in a crystal (for a more elaborate discussion, see for instance Refs. 39 and 40). The EFG is a traceless, symmetric tensor of rank 2 (5 components), and is a measure of the deviation from spherical symmetry of the electronic charge density around the nucleus under consideration. In its principal axis system (PAS), the EFG tensor is diagonal with diagonal elements  $V_{xx}$ ,  $V_{yy}$  and  $V_{zz}$  and  $V_{xx}+V_{yy}+V_{zz} = 0$  (traceless, hence specifying 2 out of the 3 quantities is enough). The axes of the PAS are conventionally labelled such that  $|V_{zz}| \geq |V_{yy}| \geq |V_{xx}|$ . Instead of specifying 2 of the 3 diagonal elements, usually the couple  $(V_{zz}, \eta)$  is specified, with  $\eta$  the so-called asymmetry parameter which equals  $(V_{xx} - V_{yy})/V_{zz}$  ( $0 \leq \eta \leq 1$ ). Often one refers with the term ‘electric-field gradient’ to  $V_{zz}$  only. Whenever we use the word ‘EFG’, we mean the tensor with its 5 components. If we mean the main component in the PAS, we write  $V_{zz}$ .

Over the past two decades, a large body of experimental results has been obtained for the EFG’s of Cd at different surfaces of Ni, Cu, Pd and Ag (see Tab. I for a summary of the experimental work, with references tracked down as much as possible to the original sources). In contrast to what the structure of Tab. I might suggest, the assignment of the experimental values to either terrace or adatom sites does not happen in a direct way. For (100) and (111) surfaces, it is easy to separate terrace and adatom sites from all other ones (steps, kinks) due to the axial symmetry ( $\eta = 0$ ) of the EFG and the perpendicular orientation of the z-axis of its PAS. It is much harder to deduce which of both is the terrace site and which one is the adatom site. Only for a few cases a thorough experimental analysis has been performed: Ag(100)<sup>44</sup> and Pd(111)<sup>40,48</sup>. Arguments include the thermal annealing behavior, the fraction of different sites dependent on the type of vicinal cut, and not at least a comparison with early ab initio cluster calculations.<sup>22,23</sup> Apart from these two well-tested cases, the partial information from thermal annealing behavior only (Cu(111)<sup>45</sup>) or from agreement with cluster calculations only (Cu(100)<sup>45</sup>) further supports the assignment in Tab. I. To our knowledge, the results on Pd(110) are published only recently and in an indirect way (unpublished Ref. 46, mentioned in Ref. 25). Prior to this information, Tab. I was commonly summarized by the following practical ‘rule’: *on a metal surface, a large  $V_{zz}$  for Cd indicates the terrace site, while a low  $V_{zz}$  indicates the adatom site.* This rule has been applied e.g. by Potzger et al.<sup>19</sup> to assign the adatom and terrace sites on Ni(100) and Ni(111). If the rule would be not universal, this site assignment could be wrong, and consequently also the conclusion on the parabolic coordination number dependence of the Cd-HFF (Fig. 3 and Section IV 1). Therefore, we will first examine the validity of this rule. Is it really valid for all (100) and (111)

TABLE I: Experimental absolute values of the principal component  $|V_{zz}|$  of the electric-field gradient tensor of Cd at various metallic surfaces, with references tracked down as much as possible to the original sources. Units:  $10^{21}$  V/m<sup>2</sup>. The lowest available measurement temperatures were chosen, and are specified below (0 K if a reliable extrapolation was available).

	Ni	Cu	Pd	Ag
(100) terrace	8.2 <sup>a b</sup>	10.3 <sup>c</sup>	8.2 <sup>d</sup>	7.5 <sup>e</sup>
(100) adatom	2.8 <sup>f</sup> / 0.3 <sup>g</sup>	0.8 <sup>h</sup>	2.8 <sup>i</sup>	0.3 <sup>j</sup>
(110) terrace	–	7.9 <sup>k</sup>	7.9 <sup>l</sup>	7.0 <sup>m</sup>
(110) adatom	–	–	8.5 <sup>n</sup>	–
(111) terrace	11.5 <sup>o</sup> / 12.3 <sup>p</sup>	10.2 <sup>q</sup>	10.2 <sup>r</sup>	8.6 <sup>s</sup>
(111) adatom	1.0 <sup>t</sup>	–	0.4 <sup>u</sup>	–

<sup>a</sup>unpublished Ref. 41, mentioned in Refs. 24 and 6

<sup>b</sup>Ref. 6, T=270-300 K

<sup>c</sup>Ref. 39, T=0 K

<sup>d</sup>Ref. 42,  $\eta = 0.16$  (!), T=0 K

<sup>e</sup>Ref. 43, T=0 K

<sup>f</sup>unpublished Ref. 41, mentioned in Ref. 24

<sup>g</sup>unpublished Ref. 41, mentioned in Ref. 19

<sup>h</sup>Mentioned in Ref. 23: private communication from G. Schatz

<sup>i</sup>Ref. 42, T=77 K

<sup>j</sup>Ref. 44, T=77 K

<sup>k</sup>Ref. 45,  $\eta = 0.74$ , T=0 K

<sup>l</sup>unpublished Ref. 46, mentioned in Ref. 25.  $\eta = 0.97$

<sup>m</sup>Ref. 43,  $\eta = 0.80$ , T=77 K

<sup>n</sup>unpublished Ref. 46, mentioned in Ref. 25.  $\eta = 0.42$

<sup>o</sup>Ref. 5, T=0 K

<sup>p</sup>Ref. 19, T=340 K

<sup>q</sup>Refs. 47 and 45, T=0 K

<sup>r</sup>Ref. 48 and 40, T=77 K

<sup>s</sup>Ref. 43, T=0 K

<sup>t</sup>Ref. 19, T=36 K

<sup>u</sup>Ref. 48 and 40, T=77 K

surfaces of the nonmagnetic metals Cu, Pd and Ag (i.e. also for the cases that are not experimentally tested in detail)? Can the rule be transferred without changes to the magnetic metal Ni? And is it really true only for (100) and (111) surfaces, and not for (110) (as the recent Pd information suggests)? Finally, what is the physical mechanism that lies behind this rule?

In response to these questions, we present in Tab. II(a) the calculated  $V_{zz}$  for both relaxed and unrelaxed structures, together with their assigned experimental values (taken from Tab. I). We did not find in the literature any experimental investigation for Cd at the Ni(110) surface. Instead, for a qualitative comparison, the data for Cd at the Pd(110) surface are enclosed in parenthesis in Tab. II(a). We also include the results obtained with the cluster method by B. Lindgren.<sup>25</sup> Unfortunately, the cluster calculations of Lindgren spanned all the orientations only for the Cu surface, while for Cd on Ni only the terrace sites at Ni(100) and (111) surfaces have been simulated. Results for Cu and Pd surfaces are therefore included in Tab. II(a) in parentheses as well. We recall here that differently to the cluster results of Lindgren, our calculations are for bulk slabs and not for non-periodic clus-

TABLE II: (a) Column 1: unrelaxed slab calculations for  $V_{zz}$  of Cd on Ni surfaces. Column 2: idem, but relaxed. Column 3: unrelaxed cluster calculations for  $V_{zz}$  of Cd on Ni surfaces, when available. If no values were available, results for Cu or Pd surfaces are given instead. Column 4: Absolute value of the experimental  $V_{zz}$  for Cd on Ni surfaces, if available (if not, values for a Pd surface are given). (b) Relaxed slab calculations for  $V_{zz}$  of Cd in terrace and adatom sites at one magnetic and three nonmagnetic (100) surfaces (sign included), compared with the absolute value of the corresponding experimental  $V_{zz}$ . Units:  $10^{21}$  V/m<sup>2</sup> everywhere.

(a)

	APW+lo		Cluster Calc.	Exp.]
	Unrelax.	Relax.	Ref.[25]	(see Tab. I)
(100) Terrace	10.5	8.6	11.0	8.2
(100) Adatom	4.0	1.9	(-0.8) <sub>Cu</sub>	2.8/0.3
(110) Terrace	9.5	-9.7	(11.2) <sub>Pd</sub>	(7.9) <sub>Pd</sub>
(110) Adatom	-9.3	-6.4	(-8.3) <sub>Pd</sub>	(8.5) <sub>Pd</sub>
(111) Terrace	10.8	13.0	16.5	11.5/12.3
(111) Adatom	-1.4	-2.9	(-6.2) <sub>Cu</sub>	1.0
(110) Terrace	$\eta = 0.83$	$\eta = 0.74$	$\eta_{Pd} = 0.97$	$\eta_{Pd} = 0.97$
(110) Adatom	$\eta = 0.18$	$\eta = 0.23$	$\eta_{Pd} = 0.28$	$\eta_{Pd} = 0.42$

(b)

	(100) terrace		(100) adatom	
	APW+lo	Exp.]	APW+lo	Exp.]
Ni	8.6	8.2	1.9	2.8/0.3
Cu	9.9	10.3	-2.0	0.8
Pd	9.1	8.2	3.4	2.8
Ag	8.5	7.5	0.4	0.3

ters. Moreover we do a ‘full’ relaxation of all the atomic positions in the cell, while due to insufficient accuracy of the method, no real forces have been calculated by Lindgren: the distance between Cd and the surface was fixed at the experimental distance, and the surrounding Ni atoms were kept in their ideal *fcc* positions (in contrast to this, the Cd atom in our *unrelaxed* calculations was at an ideal *fcc* lattice site). Our fully relaxed results compare generally very well with the experiments, predicting for (100) and (111) a low  $V_{zz}$  (close to zero) for all adatom sites, and a considerably higher  $V_{zz}$  for the terrace site, in compliance with the experimental rule. For the (110) surface, terrace and adatom sites have a comparable  $V_{zz}$ , again in agreement with the experimental observation. Taking into account the rather different approximations, there is also reasonable agreement between our unrelaxed slab calculations and the unrelaxed cluster results, the former being generally closer to experiment (especially for (111)). For the (110)-surface, the EFG is not axially symmetric ( $\eta \neq 0$ ). Values for  $\eta$  are included

in Tab. II(a) as well. Relaxation can be seen to have a moderate influence on  $\eta$ , and the considerably larger  $\eta$  in terrace sites as seen in experiments, is well-reproduced. Direct comparison with experimental values for  $\eta$  is difficult with the present data set, however (no experiments for Ni(110) and no relaxed calculations for Pd(110)).

For the (110) terrace site we observe a change in the sign of  $V_{zz}$ , when moving from the unrelaxed to the relaxed system. This is readily explained as follows.  $V_{zz}$  is defined as the largest component of the electric field gradient tensor in its principal axis system. But it might happen that there are two components of similar size, that have then necessarily opposite signs and yield a large asymmetry parameter  $\eta$  (=close to 1). This is exactly what we found for the (110) terrace case. There is a large positive component along the normal on the (110) surface, while an almost as large negative component exists along the  $[\bar{1}10]$  direction in the (110) plane. Upon relaxation the latter negative component becomes in absolute value larger than the positive one, and the latter axis becomes the one along which  $V_{zz}$  is defined. In the adatom case, the z-axis is the  $[001]$  direction in the (110) plane. Experiments on the Ni(110) surface predict instead the EFG z-axis to lay along the normal to the (110) plane. This apparent deviation between experiment and calculation is only a consequence from the way how  $V_{zz}$  is defined, not from a real discrepancy. For the other two substrate orientations, (110) and (111), the asymmetry parameter  $\eta$  is zero and there is therefore no doubt on which component is the largest one: we find in all cases the principal axis along the surface normal, as in experiment.

Having verified that the practical site assignment rule is valid for magnetic Ni(100) and Ni(111) surfaces, and not for Ni(110), we now examine for one type of surface – (100) – whether other elemental metal substrates show the same behavior. Tab. II(b) shows the calculated and experimental  $V_{zz}$  at the (100) surfaces of Ni, Cu, Pd and Ag. The calculations are in very satisfying agreement with the experiments, and it is safe now to conclude that the EFG in all of these 24 surface sites behaves in the same way.

Finally, we search for the physical mechanism that is responsible for this systematic behavior. Instead of considering for this the Ni-calculations from Tab. II, we calculated the EFG of Cd at a complete set of unrelaxed Pd-surfaces. This avoids the complication of an EFG coming from spin up and spin down electrons, and it allows for a more direct comparison with experiment because for Pd all six cases are measured (Tab. I). It does not harm not to consider relaxation here, because now we are looking for a global mechanism, not for fine details. The results are given for every diagonal component of the EFG separately in Tab. III, together with the corresponding experimental components (mind the unconventional labelling of the axes, as specified in the caption of Tab. III). Considering the fact that these are unrelaxed calculations, they reflect the experimental trend very well and hence

TABLE III: The three calculated ( $V_{ii}^{\text{calc}}$ , unrelaxed) and experimental ( $V_{ii}^{\text{exp}}$ , see Tab. I for references) components of the EFG tensor in its PAS for Cd at 6 Pd surface sites. Units:  $10^{21}$  V/m<sup>2</sup>. The usual convention for labelling the axes of the PAS is *not* followed: the z-axis is perpendicular to the surface, x- and y-axes are in the surface plane. For (100) and (111) surfaces, all directions in the surface plane are equivalent for the EFG. For the (110) surface, our x-axis refers to the  $[1\bar{1}0]$  direction, and our y-axis to the  $[001]$  direction. The principal component – which would be labelled  $V_{zz}$  in the usual convention – is printed in bold. The sign of the experimental values was not measured, but is chosen here to agree with the calculations (for the small numbers for NN=3, this is nothing more than a guess). The number of Cd-5p electrons split into  $n_{p_x}^{\text{calc}}$ ,  $n_{p_y}^{\text{calc}}$  and  $n_{p_z}^{\text{calc}}$  is given as well.

	# NN	$V_{xx}^{\text{calc}}$	$V_{yy}^{\text{calc}}$	$V_{zz}^{\text{calc}}$	$V_{xx}^{\text{exp}}$	$V_{yy}^{\text{exp}}$	$V_{zz}^{\text{exp}}$	$n_{p_x}^{\text{calc}}$	$n_{p_y}^{\text{calc}}$	$n_{p_z}^{\text{calc}}$
(111) terrace	9	-4.8	-4.8	<b>9.6</b>	-5.1	-5.1	<b>10.2</b>	0.1478	0.1478	0.0952
(100) terrace	8	-4.4	-4.4	<b>8.8</b>	-4.1	-4.1	<b>8.2</b>	0.1321	0.1321	0.0876
(110) terrace	7	-7.6	-0.5	<b>8.1</b>	-7.8	-0.1	<b>7.9</b>	0.1214	0.0986	0.0736
(110) adatom	5	2.0	<b>-6.2</b>	4.2	-2.5	-6.0	<b>8.5</b>	0.0681	0.0972	0.0651
(100) adatom	4	-1.4	-1.4	<b>2.8</b>	-1.4	-1.4	<b>2.8</b>	0.0645	0.0645	0.0580
(111) adatom	3	0.4	0.4	<b>-0.8</b>	0.2	0.2	<b>-0.4</b>	0.0424	0.0424	0.0574

these Pd-surfaces form a reliable model system to search for the physical mechanism.

Already in the very first successful *ab initio* calculations of EFG's in metals, it has been shown that magnitude and sign of the principal component  $V_{zz}$  are reflected in the so-called asymmetry count  $\Delta n_p$  of the p-electrons (for Cd, the completely filled d-shell does not contribute to the EFG). The asymmetry count is defined as  $\Delta n_p = \frac{1}{2}(n_{p_x} + n_{p_y}) - n_{p_z}$ , with  $n_{p_i}$  the number of electrons in the  $p_i$ -orbital (see Ref. 49 for the first analysis, and e.g. Refs. 50,51,52,53 for applications): spherical symmetry ( $n_{p_x} = n_{p_y} = n_{p_z}$ ) leads to  $\Delta n_p = 0$  (hence  $V_{zz} = 0$ ), charge accumulation along the z-axis ( $n_{p_x}$  large) leads to  $\Delta n_p < 0$  (hence  $V_{zz} < 0$ ), etc. For our analysis, we slightly extend this idea and take as a working hypothesis that sign and magnitude of *any* diagonal component  $V_{ii}$  is reflected in a *generalized* asymmetry count  $\Delta n_p^i = \frac{1}{2}(n_{p_j} + n_{p_k}) - n_{p_i}$  (and cyclic permutations). This hypothesis is checked by Fig. 1(a), where the calculated  $V_{ii}$  from Tab. III (right scale) are compared with the asymmetry counts  $\Delta n_p^i$  derived from the calculated number of  $p_i$  electrons in Tab. III (left scale). With the right choice of scales in Fig. 1(a), the  $\Delta n_p^i$  and  $V_{ii}$  data points almost coincide, which means that apart from a unique scaling factor both quantities reflect basically the same behavior. This proves our working hypothesis: the observed behavior of the components of the EFG is nothing more than a manifestation of the properties of the distribution of the Cd 5p-electrons over the x-, y- and z-directions. Hence, if we understand the behavior of the  $n_{p_i}$  in Tab. III, we understand the EFG. This greatly facilitates our search, as – in contrast to the  $V_{ii}$  – the  $n_{p_i}$  have a direct and intuitively understandable relation to the chemical bonds between Cd and its Pd neighbors.

The coordination dependence of the  $n_{p_i}$  is visualized in Fig. 1(b), together with a least squares fit. The picture is complicated a bit by the fact that  $n_{p_x}$  and  $n_{p_y}$  are not identical to each other for (110) surfaces. To make the

discussion more transparent, we will therefore first assume a hypothetical (110) surface with axial symmetry ( $\eta = 0$ ) for which  $n_{p_x} = n_{p_y}$  (gray symbols in Fig. 1, they are the average of the calculated  $n_{p_x}$  and  $n_{p_y}$ ). We now clearly see an almost linear dependence of  $n_{p_x}$  (or  $n_{p_y}$ ) and  $n_{p_z}$  on NN (least squares fit in Fig. 1(b)): both  $n_{p_x}$  ( $n_{p_y}$ ) and  $n_{p_z}$  decrease linearly while reducing the coordination, the decrease being stronger for  $n_{p_x}$  ( $n_{p_y}$ ) than for  $n_{p_z}$ . If we calculate the  $\Delta n_p^i$  corresponding to the least squares fits in Fig. 1(b), we obtain the straight lines in Fig. 1(a) (for overall axial symmetry, gray symbols for NN=(5,7)): this proves that the two-slope model from Fig. 1(b) is indeed the key responsible for the observed behavior of the EFG.

Can we understand the two slopes in Fig. 1(b)? Obviously,  $n_{p_i}$  should decrease with decreasing NN: Cd has no native 5p-electrons, hence in the free atom limit (NN=0) all  $n_{p_i}$  should be zero. The reason why  $n_{p_x}$  ( $n_{p_y}$ ) grows faster with NN than  $n_{p_z}$  can be understood from looking at the partial  $p_x$ - and  $p_z$ -DOS for two extreme cases (NN=3 and NN=9, see Fig. 2). The  $p_z$ -DOS has two distinct contributions below  $E_F$ : a peak about 5 eV below  $E_F$  which nicely correlates with the s-DOS of Pd neighbors *underneath* the Cd atom, and hence indicates a vertical Pd-Cd s-p hybridization, and a second peak in the interval  $[-2, 0]$  eV that corresponds with the Pd d-DOS (Pd-Cd d-p hybridization). This second peak has almost disappeared for NN=3, which indicates that it originates mainly from Pd-neighbors in the horizontal plane. For the  $p_x$ -DOS, there is only one peak, correlated mainly with the Pd d-DOS of neighbors in the horizontal plane. When going from NN=9 to NN=3, the number of Pd neighbors in the horizontal plane quickly drops (6 for NN=9, 4 for NN=8, 2 for NN=7 and 0 for lower NN), while the number of Pd neighbors underneath Cd stays rather constant (3, 4 or 5, with the largest value for intermediate NN). Hence,  $n_{p_x}$  should quickly drop while  $n_{p_z}$  tends to stay constant, which is exactly what we observed

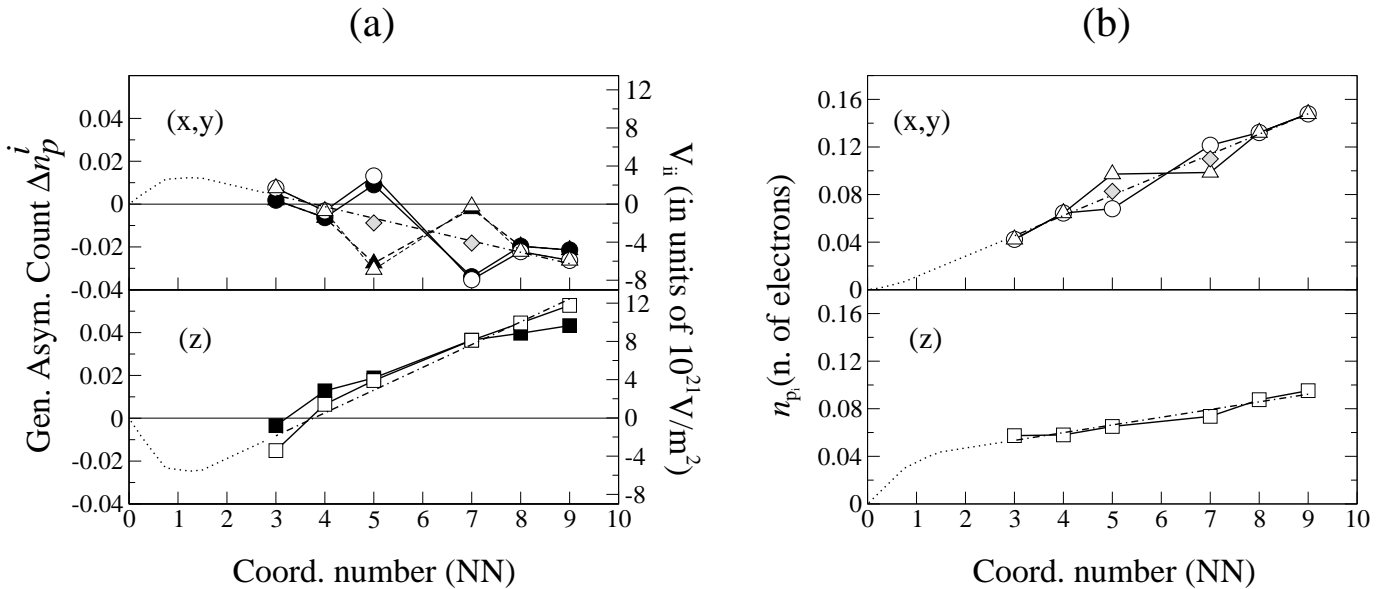


FIG. 1: (a) Black symbols: calculated components of the EFG (see Tab. III, black symbols refer to the right scale). White symbols: generalized asymmetry counts (see text), calculated from the  $n_{p_i}$  in Tab. III (white symbols refer to the left scale). Gray symbols (for (110) surfaces only): average of  $\Delta n_p^x$  and  $\Delta n_p^y$ , which would be the value of  $\Delta n_p^x = \Delta n_p^y$  in the hypothetical case of axial symmetry ( $\eta = 0$ ). Circles, triangles and squares are relative to the x,y,z components respectively of the plotted quantities. Dotted-dashed lines:  $\Delta n_p^i$  obtained from the least squares fit in Fig. 1(b). The dotted lines are calculated using the extrapolation of Fig. 1(b). (b) The  $n_{p_i}$  from Tab. III. Gray symbols (for (110) surfaces only): average of  $n_{p_x}$  and  $n_{p_y}$  in the hypothetical case of axial symmetry ( $\eta = 0$ ). Dotted-dashed lines: least squares fit, with tentative extrapolation (dotted line) to NN=0 (free atom). Both in (a) and (b) the data for the xy-plane and for the z-direction are displayed separately for clarity.

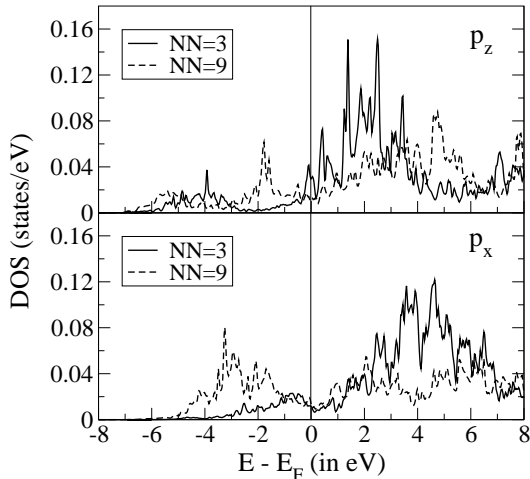


FIG. 2: Partial  $p_z$ - and  $p_x$ -DOS for unrelaxed Cd on Pd (NN=3 and NN=9).

in Fig. 1(b). Reintroducing  $\eta \neq 0$  in our discussion only redistributes the charges within the horizontal plane, and therefore does not affect our conclusion.

We emphasize that in contrast to the claimed symmetry independence of the HFF (to be discussed in Sec. IV 1), the coordination dependence of the p-

distribution for sure depends on the exact spatial arrangements of the Pd neighbors. The behavior is so smooth only because we are dealing with fairly ‘similar’ environments (Pd underneath, vacuum above). Furthermore, a tentative extrapolation of Fig. 1(b) to very low coordination sites (NN=1, 2) suggests a negative  $V_{zz}$  there. This is confirmed for the NN=2 environment for Cd on Ni to be discussed in Tab. III, where we calculate  $V_{zz} = -2.4 \cdot 10^{21} \text{ V/m}^2$ .

In contrast to the discrete behavior suggested by the practical rule (‘terrace site means large  $V_{zz}$ , adatom site means low  $V_{zz}$ ’), we conclude that there is a continuous evolution as a function of the coordination number. The (100) and (111) terrace sites are both highly coordinated, and therefore have indeed the largest  $V_{zz}$ , while the opposite is true for the (100) and (111) adatom sites. The (110) terrace and adatom sites have intermediate coordination – and therefore comparable  $V_{zz}$ ’s – which is why the ‘rule’ does not seem to work for (110). However, there is nothing exceptional about the (110) surface.

#### IV. MAGNETIC HYPERFINE FIELDS

We now limit ourselves to Ni surfaces again and discuss the results obtained for the hyperfine fields. Two main questions will be addressed. First, we want to verify

and understand the experimentally proposed parabolic dependence of the Cd HFF on the number of Ni neighbors in the first coordination shell (NN), and we examine whether and how the spatial arrangement of these neighbors influences the HFF. As a second problem, we broaden the scope to the entire 5sp series, placing 5sp impurity atoms only in NN=4 (adatom) and NN=8 (terrace) coordinated sites at the Ni(100) surface. This will allow us to generalize the behavior observed for Cd to other probe atoms, and to propose qualitative explanations on the mechanisms ruling the observed HFF's.

### 1. Cd HFF's on Ni surfaces

In this section we focus on Cd probe atoms, placed in terrace and adatom positions at the three low-Miller-index surface of *fcc* Ni. This gives access to 6 differently coordinated sites, in addition to the fully coordinated substitutional bulk site and to a more artificial bridge site with NN=2. In order to test the sensibility of the HFF on the details of the cells, we performed also several calculations by varying the cell size and number of Ni layers in the slab. All the calculated Cd HFF for the differently coordinated systems are summarized in Table IV. Details on the cell are given in the format: (2D cell size, number of Ni layers). The Cd-Cd distance through the vacuum spacer is given in parentheses besides the HFF values. The long hyphen '-' is used to label cases that were not calculated. The NN=2 coordinated site has been achieved by placing the Cd atom in a non-crystallographic adatom position on Ni(111). An 'ideal unrelaxed position' has therefore no meaning for Cd on this site, which is indicated by the label 'n.p.' ('not possible'). For the fully coordinated bulk site, (NN=12) both a bulk and a slab calculation are reported, the latter with the Cd placed in the middle layer of the Ni slab. The experimental results of Potzger<sup>19</sup> are reported in the last column. We first discuss the unrelaxed calculations, where all the atoms (including Cd) sit at their ideal *fcc* position. The calculated values predict for the Cd HFF a change in sign for mid coordination and large positive values for low coordination, in agreement with the experimental assignments. Changing the size of the slab, by adding Ni layers or by increasing the extension of the cells in the surface plane, results into some scattered values which lay, except for NN=5 and to a lesser extent also for NN=4, within the aforementioned expected precision ( $\pm 5$ T). For the NN=5 case, i.e. adatom position at the Ni(110) surface, the HFF's are found to attain large negative values for some of the considered cells. We will come back to these puzzling results later on.

As already discussed before, lattice relaxations are expected in such open systems and might induce important changes to the HFF's. In fact it has been shown recently that their inclusion improves the agreement with the experimental data, in the case of 5sp and 6sp impurities in bcc bulk Fe.<sup>10,11</sup> Due to the larger atomic volume of

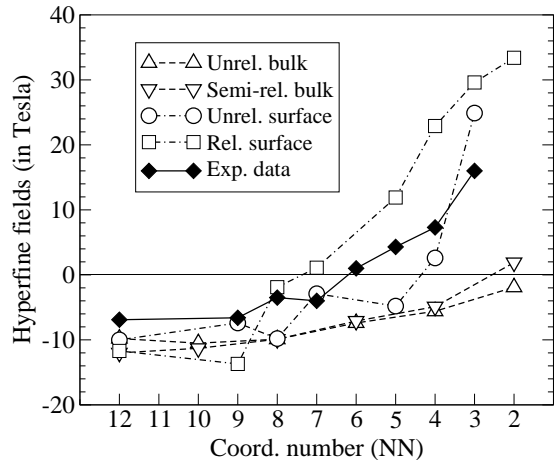


FIG. 3: Calculated coordination number (NN) dependence of the Cd hyperfine field. Details are explained in the text.

Cd with respect to Ni, an outward relaxation away from the surface is expected for both terrace and adatom positions, for all low-index surfaces. Our calculations show Cd displacements from ideal *fcc* positions towards the vacuum, that range from 0.60 to 0.90 Å for the terrace atom and from 0.09 to 0.26 Å for the adatom, depending on the surface orientation (Tab. V). Displacements for the terrace site are larger than for the adatom site: the Cd atom strives for a Cd-Ni bond length of about 2.65 Å that is somewhat larger than the ideal *fcc* Ni-Ni bond length of 2.48 Å. Starting from an adatom position, this can be realized with less displacement. Minor relaxations appear also in the Ni atoms around the impurity. As evident from Tab. IV, the correction due to the relaxation is mostly within 7 T (except for NN=4 with corrections up to 35 T, see later). The correction is negative for the highest coordination numbers (NN=9 and 12) and positive for all others.

For a better comparison, the theoretical results for the unrelaxed and relaxed systems are plotted in Fig. 3 together with the experimental results. When more than one value exists in Tab. IV, the ones relative to the cell with the largest volume are selected, except for the more sensitive NN=4 and NN=5 cases where the values closer to the experiments are chosen (this will be justified below). The chosen HFF's are given in bold in Tab. IV. As evident from Fig. 3, upon relaxation of the atoms in the cell the barycenter of the HFF curve moves towards more positive values for NN > 9, inducing a sign change already for NN = 7 (Cd on a Ni(110) terrace site). The largest changes are seen for NN=4 and NN=5, indicating once more a high sensitivity of these environments. No clear overall improvement is found when relaxations are included, and the experimental data lays somehow between the relaxed and unrelaxed theoretical curves.

In order to investigate the reason for the large variations seen for the NN=4 and NN=5 coordinated sites, it is fruitful to look at the partial Density Of States (DOS)

TABLE IV: Hyperfine fields (T) of Cd in different Ni-environments. Experimental values are taken from Ref. 19

	# NN	Type of cell	Hyperfine fields (in T)		Exp
			non-relaxed	relaxed	
Bulk	12	(2 × 2 × 2)	<b>-9.8</b>	<b>-12.0</b>	-6.9
(100) Bulk		(2 × 2, 7L)	-10.0	-11.7	
(111) Terrace	9	( $\sqrt{2} \times \sqrt{2}$ , 7L)	<b>-7.4</b> (12.18 Å)	<b>-13.7</b> (10.49 Å)	-6.6
(100) Terrace	8	(2 × 2, 5L)	-9.8 (7.02 Å)	-1.9 (5.80 Å)	-3.5
		(2 × 2, 7L)	<b>-8.3</b> (7.02 Å)	<b>-6.7</b> (5.82 Å)	
		( $\sqrt{2} \times \sqrt{2}$ , 7L)	-3.6 (13.19 Å)	-5.9 (11.88 Å)	
bulk-like ('random')		(2 × 2 × 2)	-9.9	—	
bulk-like (terrace)		(2 × 2 × 2)	-8.2	—	
<i>bcc</i> -bulk		(2 × 2 × 2)	-8.9	—	
(110) Terrace	7	(2 × $\sqrt{2}$ , 7L)	<b>-2.9</b> (7.45 Å)	<b>1.1</b> (5.66 Å)	
		(2 × 2 $\sqrt{2}$ , 9L)	-6.8 (7.45 Å)	—	
(110) Adatom	5	(2 × $\sqrt{2}$ , 5L)	<b>-4.8</b> (7.45 Å)	<b>11.9</b> (6.91 Å)	4.3
		(2 × $\sqrt{2}$ , 7L)	-14.2 (7.45 Å)	-6.5 (6.93 Å)	
		(2 × 2 $\sqrt{2}$ , 7L)	-21.7 (7.45 Å)	—	
(100) Adatom	4	(2 × 2, 5L)	-6.5 (7.02 Å)	-3.6 (6.51 Å)	7.3
		(2 × 2, 7L)	3.4 (7.02 Å)	38.7 (6.63 Å)	
		( $\sqrt{2} \times \sqrt{2}$ , 5L)	—	15.9 (9.35 Å)	
		( $\sqrt{2} \times \sqrt{2}$ , 7L)	<b>2.6</b> (9.67 Å)	<b>22.9</b> (9.28 Å)	
		( $\sqrt{2} \times \sqrt{2}$ , 9L)	—	31.9 (9.35 Å)	
		( $\sqrt{2} \times \sqrt{2}$ , 11L)	—	25.1 (9.35 Å)	
bulk-like ('random')		(2 × 2 × 2)	-5.6	—	
bulk-like (adatom)		(2 × 2 × 2)	8.0	—	
bulk-like (free layer)		(2 × 2 × 2)	-4.2	—	
<i>bcc</i> bulk like (adatom)		(2 × 2 × 2)	-9.6	—	
(111) Adatom	3	(2 $\sqrt{2} \times 2\sqrt{2}$ , 5L)	<b>24.9</b> (8.11 Å)	<b>31.9</b> (7.92 Å)	16.0
(111) Adatom	2	( $\sqrt{2} \times \sqrt{2}$ , 7L)	n.p.	<b>33.4</b> (8.26 Å)	—

TABLE V: Cd perpendicular relaxations (in Å) from ideal *fcc* crystallographic site for the three low-index Ni surfaces. Everywhere Cd moves towards the vacuum.

Site	(100)	(110)	(111)
Adatom	0.20	0.26	0.09
Terrace	0.60	0.90	0.84

of Cd with *s*-symmetry (only *s*-electrons contribute to the HFF). In Fig. 4 the majority and minority *s*-DOS of a Cd adatom on Ni(100) is shown in a small energy window in the vicinity of the Fermi energy. Since it is not clear *a priori* whether the problem arises due to the adopted approximation for the exchange-correlation functional, LDA-calculations are presented as well. The *s*-DOS shows several structures, among them a pronounced peak which for the majority channel lays right at  $E_F$  while it remains above  $E_F$  for the minority channel. Small variations in the details of the cell (number of layers, 2D

cell size, relaxation or not, ...) or in the computational method (LDA/GGA, APW+lo or KKR, ...) will push this peak in the majority channel below or above  $E_F$ . Since only the majority spin is involved, one has a net change of the *s* spin magnetic moment, and – because this is roughly proportional to the HFF – also a change of the HFF itself. For instance, in the two examples in Fig. 4, the *s* spin moment and HFF are  $2.02 \cdot 10^{-2} \mu_B$  and 38.7 T for GGA, and  $1.05 \cdot 10^{-2} \mu_B$  and 20.4 T for LDA. We pinpoint here that the LDA does not generally solve this sensitivity problem: in the NN=5 adatom unrelaxed case, for instance, similar negative *s* moments and large negative HFF are obtained both by LDA and GGA. As a general rule, whenever such a peak is observed so close to  $E_F$ , an enhanced sensitivity of the HFF is foreseen, which adds to the inner precision of the calculations. For NN=4 and NN=5, we do observe such a peak in the *s*-DOS, for the other environments this is not the case. This explains the instability and wide scattering of the HFF's for those two coordination numbers in Tab. IV (note that this instability does not affect the calculations for  $V_{zz}$ , which



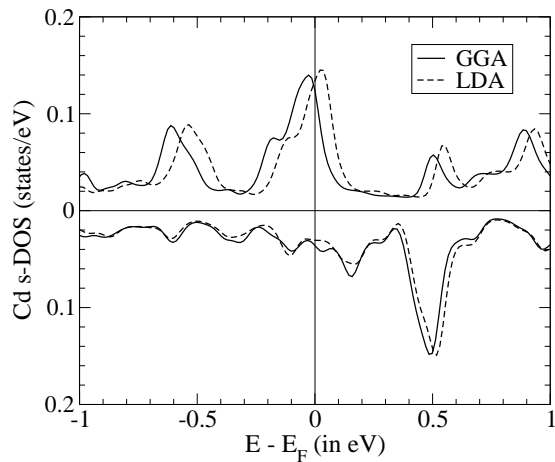


FIG. 4: Partial s-DOS for relaxed Cd on Ni(100) calculated in the LDA and GGA approximations.

are ruled by p- rather than s-electrons). For impurity elements other than Cd, it might be that such sensitivity does not show up at all, or – if it does – it might do so for other values of the coordination number, depending on the details of the s-DOS close to  $E_F$ . The experimental values in Tab. IV are up to 20 T below the calculated values for  $NN \geq 4$ . This indicates that in nature the majority s-peak is above  $E_F$ , while in our calculations it is below.

We now turn to the experimental parabolic NN-counting rule from Fig. 3. Both our relaxed and unrelaxed calculations show roughly the same trend (Fig. 3), and agree with the experimental trend. But how absolutely does this ‘parabolic rule’ holds? Is it really true – as concluded by Potzger et al.<sup>19</sup> – that knowledge of the NN coordination is enough to predict the HFF on Cd in Ni-environments? In order to answer this question, we exploit the advantage of *ab initio* calculations that one is not restricted to environments that necessarily have to exist in nature. We can easily create artificial Cd-in-Ni-environments with an arbitrary number of nearest neighbors. That allows us to test the NN-counting rule in more situations than are experimentally accessible. The environments we created are  $2 \times 2 \times 2$  supercells for Cd in Ni, with a given amount of nearest neighbor Ni atoms removed (such that vacancies remain). This removal was done pair by pair, with the requirement that the remaining cell still has inversion symmetry (out of the several possibilities for every NN, we calculated only one). This requirement makes such environments essentially different from the corresponding surface environments with the same NN, because the latter inevitably do not have inversion symmetry. In a first series, we start from the relaxed Cd-in-Ni supercell (labelled as ‘semi-relaxed’, because after removal of the Ni atoms no further relaxation is done), in a second series all atoms are at the ideal Ni bulk positions. The results of both series are almost identical, and are reported in Fig. 3. Clearly, the same

trend as in experiment and as in the surface calculations is present in the artificial bulk calculations. This proves that there is a basic truth in the NN-counting rule. On the other hand, the large difference between the bulk and surface calculations – especially for the low-coordination environments – is a clear sign that contributions from higher coordination shells are not negligible.

If the requirement of inversion symmetry is removed, we can bridge the gap between these bulk-like cases and the surface slabs by calculating bulk-like cells where the first coordination shell is exactly the same as on a specific surface site. We did this for  $NN=8$  and  $NN=4$  (Tab. IV, the environment labelled as ‘random’ is the one with inversion symmetry). For  $NN=8$ , we could simulate in this way an environment that has exactly the same NN-coordination as the (100) terrace site. If the NN-counting rule were absolutely valid, we would find exactly the same HFF in the random and terrace-like bulk case. The results are indeed quite close:  $-9.9$  T and  $-8.2$  T, which are values that are also not far from the slab calculation ( $-8.3$  T). An even more daring test of the counting rule, is to put Cd at a substitutional site of an unrelaxed hypothetical *bcc* Ni  $2 \times 2 \times 2$  supercell (16 atoms), with a lattice constant chosen such that the Ni-Ni distance (and hence also the unrelaxed Cd-Ni distance) is the same as in the *fcc* case. Even in this very different kind of environment, the calculated HFF of  $-8.9$  T follows the simple counting rule. All this is different for  $NN=4$ . Apart from the random environment ( $-5.6$  T), we tested a configuration that is identical to the *fcc* (100) adatom case (8.0 T), a configuration with all 4 Ni plus Cd in the same plane (a free layer,  $-4.2$  T), and in a *bcc* cell a configuration that is identical to a *bcc* (100) adatom ( $-9.6$  T). These 4 numbers prove that – even in *fcc*-based environments only – the exact spatial configuration of the Ni neighbors in the first coordination shell can be important, leading to differences of more than 13 T. It is not surprising to find this effect for  $NN=4$  rather than  $NN=8$ , the former being identified before as a sensitive case. From this analysis we conclude that although the NN-counting rule certainly indicates a trend, there can be substantial deviations from it for specific environments. In such sensitive environments, the spatial arrangement of the neighbors is important as well. There is probably some luck involved that for Cd in Ni the behavior in nature is so smooth as experimentally observed, and there is no fundamental reason why the data could not have been considerably more scattered around the parabolic trend.

## 2. HFF’s of the 5sp series

As a last part of this study we now present a survey for the 5sp impurities from Cd to Ba in Ni-environments, to see if and how the NN-counting rule can be extended to other impurities. We use the strategy applied by Mavropoulos et al.<sup>26</sup> for 4sp impurities on Fe and Ni surfaces, and very recently and independently from this

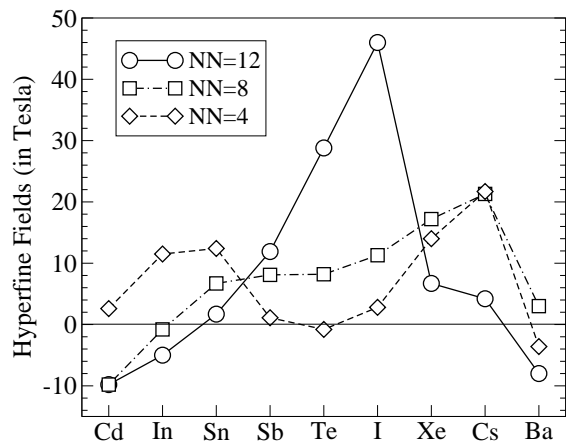


FIG. 5: Hyperfine fields of the whole 5sp series (Cd  $\rightarrow$  Ba) in bulk Ni (circle, NN=12), at a terrace position (squares, NN=8) and at an adatom position (diamonds, NN=4) on the Ni(100) surface.

work also for 5sp impurities on Ni surfaces.<sup>27</sup> We take the bulk environment (NN=12) and the terrace (NN=8) and adatom (NN=4) environments for the (100) surface, and calculate the HFF for the 9 elements from Cd to Ba in those environments. The cell sizes chosen for those calculations are the ones labelled as in Tab. IV as  $(2 \times 2 \times 2)$ ,  $(2 \times 2, 5L)$  and  $(2 \times 2, 7L)$ , respectively. Because we are looking again for gross trends now and not for fine details, relaxations were not included. The results for the 5sp HFF's are displayed in Fig. 5. Exactly the same behavior as Mavropoulos et al. observed for 4sp and 5sp impurities is seen here, which mutually supports the validity of the very different computational methods that were used. In the bulk environment, the HFF starts at about  $-10$  T for Cd, strongly increases with increasing atomic number  $Z$ , and reaches a maximum near the middle of the series:  $\approx 46$  T for I. Then it decreases again, and at the end of the series turns back to values close to  $-10$  T. When the coordination number is reduced, the main peak of the HFF curve moves to heavier elements and an additional structure – that for NN=8 is more a broad shoulder than a peak – appears at the beginning of the series. For NN=4 two clear structures are evident, and the HFF increases and decreases (with less intense variations than for the bulk) twice in the course of the 5sp series.

The microscopic origin of Fig. 5 can be understood by a slight extension of arguments given by Mavropoulos et al.<sup>26</sup> for 4sp impurities. Later on, we will then derive (and test) generalized NN-counting rules for all 5sp impurities in Ni environments from them. For a systematic explanation, let us go back to the origin of hyperfine fields in ferromagnets (see Ref. 7 for a detailed and instructive review). As the hyperfine field in our cases is dominated by the Fermi contact contribution, we have to care about the details of the bond between the 5s states and its environment (here Ni-3d). It has been known for a long

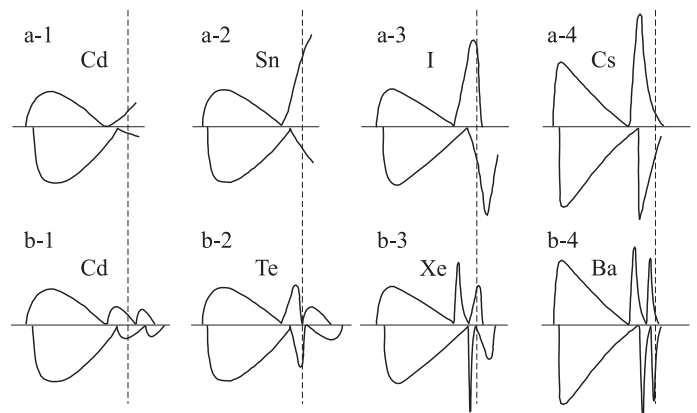


FIG. 6: Cartoons for the majority and minority partial s-DOS of (a) a 5sp impurity in bulk Ni and (b) a 5sp impurity at a Ni surface. The vertical line indicates the Fermi energy, the name of the elements indicates for which element a particular picture is representative. This picture is inspired by Ref. 7.

time<sup>54,55</sup> that in the case of such an s-d bond the local s-DOS of the impurity shows a characteristic depression a few eV below the Fermi energy: the ‘antiresonance dip’ (AR). The position of the AR is mainly determined by the host material (Ni), and not by the impurity. The states below the AR are bonding states, the states above are antibonding. The up and down states are exchange split, such that at first sight one expects an excess of s-up over s-down, resulting in a positive hyperfine field. Due to a different s-d hybridization for up and down electrons, however, the number of s-up below AR will be diminished, while the number of s-down will be enhanced. Above AR, the situation is opposite.<sup>56</sup> The final result is that the impurity s-moment (and hyperfine field) will be negative in the beginning of the sp-series, where the effect of the bonding states is dominant (Fig. 6-a-1). In the second half of the series, also the antibonding states will get filled, and because they have to be squeezed between AR and the Fermi energy, they have to develop a sharp peak in the DOS. The exchange splitting of this peak is responsible for the large positive HFF at the end of the sp-series (Fig. 6-a-2/3), which quickly drops to small and negative values again if also the down antibonding states are below the Fermi energy (Fig. 6-a-4). Mavropoulos et al. have shown by group theoretical arguments that in the case of reduced point group symmetry for the impurity (as on surfaces), the antibonding part of the impurity s-DOS is split in two parts. This splitting is more pronounced if the impurity is in a more non-bulk-like environment, i.e. it is more pronounced for NN=4 than for NN=8. Let us take the NN=4 case with a clear splitting. When going from Cd to Ba, we evolve through the different stages of Fig. 6-b, which explains the double-peak structure of the HFF for NN=4 in Fig. 5.

An aspect of Fig. 5 that has not been discussed by Mavropoulos et al., is the physical origin of the coordi-

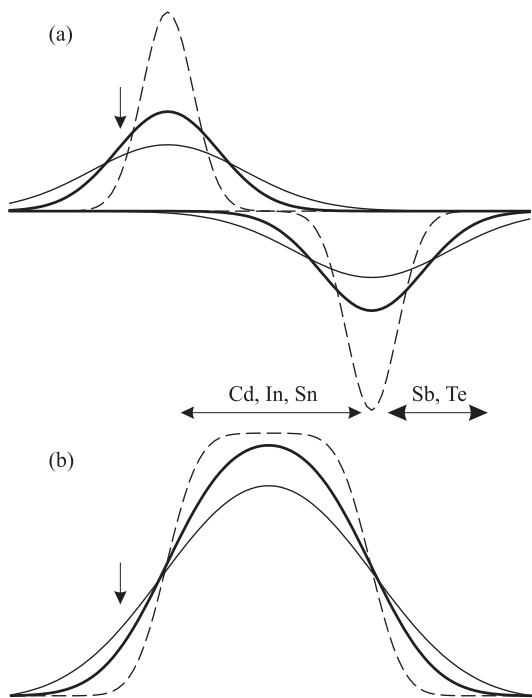


FIG. 7: (a) The first of the two antibonding s-peaks for majority and minority spin. (b) The s-moment derived from (a) by subtracting – at a particular energy – the integral of the minority s-DOS up to that energy from the integral of the majority s-DOS up to that energy. In both (a) and (b) 3 typical cases are drawn: high coordination = broad band width (thin full line), medium coordination = medium band width (thick full line) and low coordination = small band width (dashed line). The horizontal arrows indicate the region where the Fermi energy falls for the indicated elements (first half of the 5sp-series). This story can be repeated with the second of the two antibonding peaks, starting from I for which the Fermi energy falls at the place indicated by the vertical arrow.

nation number dependence of the HFF for a particular element: why is e.g. for In the NN=4 HFF the larger one and the NN=12 the smaller one, while this is reversed for e.g. Te? This we will explain by the cartoon in Fig. 7. The upper part of Fig. 7 schematically shows the first of the two antibonding s-peaks of Fig. 6-b, for any particular impurity. If one lowers the coordination number of the impurity, the band-width of these peaks will decrease – an obvious fact, which we clearly observe in our calculations. Fig. 7-a shows the same situation for 3 typical band-widths: large (NN=12), medium (NN=8) and small (NN=4). The bottom part of Fig. 7 shows the s spin moment derived from Fig. 7-a as a function of energy (found by subtracting the integral of the down-peak from the integral of the up-peak, where the integrals are made up to the energy under consideration). Everything now depends on where the Fermi energy lies in Fig. 7. If it falls in the region indicated by Cd-In-Sn, Fig. 7-a corresponds to Fig. 6-b-1. At the corresponding energy in Fig. 7-b,

the s-moment (HFF) for the small band-width (NN=4) is larger than for the medium band-width (NN=8), which in turn is larger than for the large band-width (NN=12). If the Fermi energy falls in the region indicated by Sb-Te, Fig. 7-a corresponds to Fig. 6-b-2 and the sequence of s-moments is reversed. After Te, this story repeats for the second antibonding peak (for I, the Fermi energy will be at the position marked by the vertical arrow, but of course in the second series of peaks), but will be increasingly less clear due to the presence of the 6s states that start to manifest themselves around the Fermi energy. That is the reason for the more chaotic evolution for Cs and Ba. Of course, Fig. 7 is a cartoon only, and its conclusions should not be taken too literally: the real DOS are not Gaussians as used in the cartoon, and therefore the details of the hyperfine field evolution might be different. Nevertheless, it captures the basic mechanism. Summarizing, we conclude that the physical mechanism behind Fig. 5 can be understood from a combination of three basic features: i) the double peak structure of the antibonding peaks, ii) the decrease in the band width – and hence the increase of peak height – upon reduction of the coordination number, and iii) the position of the Fermi energy with respect to the peaks.

We now take Fig. 5 as a source of inspiration to extend the parabolic NN-counting rule proposed by Potzger et al. (Ref. 19) for 5sp impurities other than Cd. It can be seen from Fig. 5 that the Cd-HFF for bulk and NN=8 is almost the same and negative, while the value for NN=4 is small and positive: this is the parabolic behavior seen in experiment. In the same way, we can then deduce that for In and Sn as impurities, the HFF should monotonically rise from NN=12 to NN=4 (it is interesting to note that for the experimentally ‘easily’ accessible Mössbauer probe  $^{119}\text{Sn}$ , Fig. 5 suggests a linear behavior). Between Sn and Sb all lines cross, such that for Sb to I the HFF monotonically decreases from NN=12 to NN=4. For Xe to Ba, there is non-monotonic behavior instead. We have checked this deduction by calculating the artificial bulk-like (non-relaxed) environments as discussed before, but now for Te and Ba as impurities (both are taken as a representative for the region of monotonic decrease and the non-monotonic region, just as Cd is a representative of the region of monotonic increase). In these bulk-like cells, we can more easily create environments with NN different from 4, 8 and 12. The results are given in Fig. 8. The general trends shown in Fig. 6 are the same as the ones which could be inferred from the surface calculations of Fig. 5: monotonic (parabolic) increase for Cd, monotonic decrease for Te and non-monotonic behavior for Ba. In the light of these results we therefore conclude that each of the 5sp impurities in Ni has its own typical coordination number counting rule.

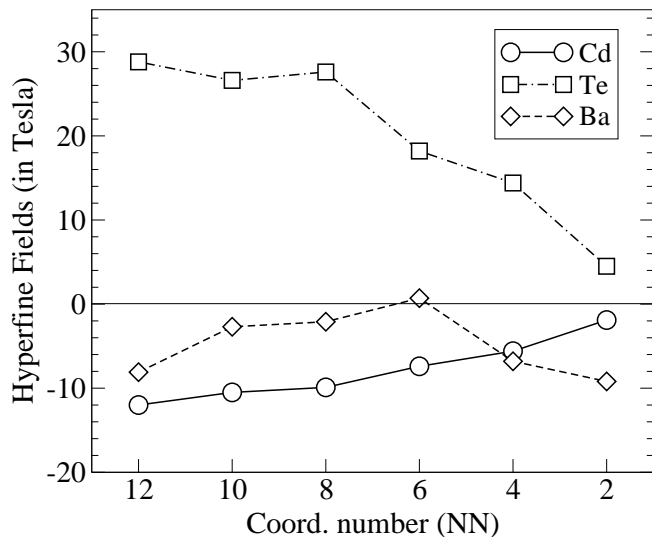


FIG. 8: Coordination dependence of the HFF for selected, i.e. Cd, Te and Ba, 5sp elements as obtained by bulk calculations (see text for details).

## V. CONCLUSIONS

We have undertaken an extensive confrontation between state-of-the-art *ab initio* calculations and a high-quality data set – experimentally collected during the past 20 years – of electric-field gradients and magnetic hyperfine fields of Cd at magnetic and non-magnetic metallic fcc surfaces. We conclude that the experimental practice for (100) and (111) surfaces of assigning a large  $V_{zz}$  to terrace sites and a low  $V_{zz}$  to adatom sites is correct. However, this ‘discrete’ rule is nothing more than a manifestation of a continuous evolution of the EFG com-

ponents as a function of coordination number, an evolution for which we have pointed out the physical mechanism. With this insight, the behavior of the (110) surface is not exceptional at all. The experimentally suggested parabolic-like coordination number dependence for the HFF of Cd at Ni surfaces is confirmed as being a reliable trend, but we warn that it is just a trend and not a rigorous rule: sensitive environments exist, for which the spatial arrangement of the Ni neighbors considerably influences the HFF. We have explained in detail the physical mechanism behind the HFF for all 5sp impurities at Ni surfaces, by combining knowledge from the literature and new insight. In particular we have generalized the parabolic NN-counting rule for Cd to other 5sp impurities, showing that each impurity has its own typical rule, and explaining why this is so. We hope to have demonstrated that *ab initio* calculations can greatly enhance the physical insight in an experimentally complex problem.

## Acknowledgments

One of the authors (V.B.) acknowledges fruitful discussion with Dr. K. Potzger. Part of the calculations were performed on computer facilities granted by an INFM project *Iniziativa Trasversale Calcolo Parallelo* at the CINECA supercomputing center. Another part of computational work was performed on computers in Leuven, in the frame of project G.0239.03 of the *Fonds voor Wetenschappelijk Onderzoek - Vlaanderen* (FWO). The authors are indebted to L. Verwilt and J. Knudts for building and maintaining the pc-cluster in Leuven. M.C. thanks the *Onderzoeksfonds* of the K.U.Leuven for granting a post-doctoral fellowship (F/02/010). Knowledge, help and advice from the active WIEN2k user community are warmly acknowledged.

\* Electronic address: Stefaan.Cottenier@fys.kuleuven.ac.be

† Electronic address: Bellini.Valerio@unimore.it

<sup>1</sup> R. Vianden, in *Nuclear Physics Application on Materials Science*, edited by E. Recknagel and J. C. Soares (Kluwer Academic Publishers, 1988), p. 239.

<sup>2</sup> G. Schatz, in *Nuclear Physics Application on Materials Science*, edited by E. Recknagel and J. C. Soares (Kluwer Academic Publishers, 1988), p. 297.

<sup>3</sup> G. Krausch, R. Fink, K. Jacobs, U. Kohl, J. Lohmüller, B. Luckscheiter, R. Platzer, B.-U. Runge, U. Wöhrmann, and G. Schatz, *Hyperfine Interactions* **78**, 261 (1993).

<sup>4</sup> H. Haas, *Z. Naturforsch.* **50a**, 407 (1994).

<sup>5</sup> J. Voigt, R. Fink, G. Krausch, B. Luckscheiter, R. Platzer, U. Wöhrmann, X. L. Ding, and G. Schatz, *Phys. Rev. Letters* **64**, 2202 (1990).

<sup>6</sup> H. H. Bertschat, H.-H. Blaschek, H. Granzer, K. Potzger, S. Seeger, and W.-D. Zeitz, *Phys. Rev. Letters* **80**, 2721 (1998).

<sup>7</sup> H. Akai, M. Akai, S. Blügel, R. Zeller, and P. H. Dederichs, *J. Magn. Magn. Materials* **45**, 291 (1984).

<sup>8</sup> S. Blügel, H. Akai, R. Zeller, and P. H. Dederichs, *Phys. Rev. B* **35**, 3271 (1987).

<sup>9</sup> H. Akai, M. Akai, S. Blügel, B. Drittler, H. Ebert, K. Terakura, R. Zeller, and P. H. Dederichs, *Progr. Theor. Phys. Suppl.* **101**, 11 (1990).

<sup>10</sup> T. Korhonen, A. Settels, N. Papanikolaou, R. Zeller, and P. H. Dederichs, *Phys. Rev. B* **62**, 452 (2000).

<sup>11</sup> S. Cottenier and H. Haas, *Phys. Rev. B* **62**, 461 (2000).

<sup>12</sup> H. Haas, *Hyperfine Interactions* **129**, 493 (2000).

<sup>13</sup> V. Bellini, R. Zeller, and P. Dederichs, *Phys. Rev. B* **64**, 144427 (2001).

<sup>14</sup> C. O. Rodriguez, M. V. Ganduglia-Pirovano, E. L. Peltzer y Blancá, M. Petersen, and P. Novák, *Phys. Rev. B* **63**, 184413 (2001).

<sup>15</sup> C. O. Rodriguez, M. V. Ganduglia-Pirovano, E. L. Peltzer y Blancá, and M. Petersen, *Phys. Rev. B* **64**, 144419 (2001).

<sup>16</sup> R. N. Nogueira and H. M. Petrilli, *Phys. Rev. B* **60**, 4120 (1999).

<sup>17</sup> S. Frota-Pessôa and S. Legoas, *Hyperfine Interactions* **133**,

- 207 (2001).
- <sup>18</sup> J. A. Gómez and D. Guenzenburger, *J. Phys.: Condensed Matter* **14**, 12311 (2002).
  - <sup>19</sup> K. Potzger, A. Weber, H. Bertschat, W.-D. Zeitz, and M. Dietrich, *Phys. Rev. Letters* **88**, 247201 (2002).
  - <sup>20</sup> M. J. Prandolini, Y. Manzhur, A. Weber, K. Potzger, H. H. Bertschat, and M. Dietrich, abstract presented at ICM2003.
  - <sup>21</sup> H. Haas, *Hyperfine Interactions* **84**, 69 (1994).
  - <sup>22</sup> B. Lindgren, *Hyperfine Interactions* **34**, 217 (1987).
  - <sup>23</sup> B. Lindgren, *Europhys. Lett.* **11**, 555 (1990).
  - <sup>24</sup> B. Lindgren and A. Ghandour, *Hyperfine Interactions* **78**, 291 (1993).
  - <sup>25</sup> B. Lindgren, *Z. Naturforsch.* **57a**, 544 (2002).
  - <sup>26</sup> Ph. Mavropoulos, N. Stefanou, B. Nonas, R. Zeller, and P. H. Dederichs, *Phys. Rev. Letters* **81**, 1505 (1998).
  - <sup>27</sup> Ph. Mavropoulos, *J. Phys.: Condensed Matter* **15**, 8115 (2003).
  - <sup>28</sup> P. Hohenberg and W. Kohn, *Phys. Rev.* **136**, 864 (1964).
  - <sup>29</sup> W. Kohn and L. J. Sham, *Phys. Rev.* **140**, A1133 (1965).
  - <sup>30</sup> P. Blaha, K. Schwarz, G. Madsen, D. Kvasnicka, and J. Luitz, *WIEN2k, An Augmented Plane Wave + Local Orbitals Program for Calculating Crystal Properties*, (Karlheinz Schwarz, Techn. Universität Wien, Austria) (1999), ISBN 3-9501031-1-2.
  - <sup>31</sup> J. P. Perdew, S. Burke, and M. Ernzerhof, *Phys. Rev. Letters* **77**, 3865 (1996).
  - <sup>32</sup> A. Settels, T. Korhonen, N. Papanikolaou, R. Zeller, and P. H. Dederichs, *Phys. Rev. Letters* **83**, 4369 (1999).
  - <sup>33</sup> H. M. Petrilli, P. E. Blöchl, P. Blaha, and K. Schwarz, *Phys. Rev. B* **57**, 14690 (1998).
  - <sup>34</sup> G. Kresse and J. Furthmüller, *Comp. Mater. Science* **6**, 15 (1996).
  - <sup>35</sup> G. Kresse and J. Furthmüller, *Phys. Rev. B* **54**, 11169 (1996).
  - <sup>36</sup> D. A. Shirley, S. S. Rosenblum, and E. Matthias, *Phys. Rev.* **170**, 363 (1968).
  - <sup>37</sup> E. Fermi, *Z. Physik* **60**, 320 (1930).
  - <sup>38</sup> P. Dufek, P. Blaha, and K. Schwarz, *Phys. Rev. Letters* **75**, 3545 (1995).
  - <sup>39</sup> T. Klas, J. Voigt, W. Keppner, R. Wesche, and G. Schatz, *Phys. Rev. Letters* **57**, 1068 (1986).
  - <sup>40</sup> E. Hunger and H. Haas, *Surf. Sci.* **234**, 273 (1990).
  - <sup>41</sup> J. Voigt, Ph.D. thesis, Universität Konstanz (1990).
  - <sup>42</sup> R. Fink, B.-U. Runge, K. Jacobs, G. Krausch, J. Lohmüller, B. Luckscheiter, U. Wöhrmann, and G. Schatz, *J. Phys.: Condensed Matter* **5**, 3837 (1993).
  - <sup>43</sup> R. Wesche, R. Fink, T. Klas, G. Krausch, R. Platzter, J. Voigt, and G. Schatz, *J. Phys.: Condensed Matter* **1**, 7407 (1989).
  - <sup>44</sup> R. Fink, R. Wesche, T. Klas, G. Krausch, R. Platzter, J. Voigt, U. Whrmann, and G. Schatz, *Surf. Sci.* **225**, 331 (1990).
  - <sup>45</sup> T. Klas, R. Fink, G. Krausch, R. Platzter, J. Voigt, R. Wesche, and G. Schatz, *Surf. Sci.* **216**, 270 (1989).
  - <sup>46</sup> G. Filleböck, private communication to B. Lindgren.
  - <sup>47</sup> T. Klas, R. Fink, G. Krausch, R. Platzter, J. Voigt, R. Wesche, and G. Schatz, *Europhys. Lett.* **7**, 151 (1988).
  - <sup>48</sup> E. Hunger, H. Haas, and H. Grawe, *Hyperfine Interactions* **60**, 999 (1990).
  - <sup>49</sup> P. Blaha, K. Schwarz, and P. H. Dederichs, *Phys. Rev. B* **37**, 2792 (1988).
  - <sup>50</sup> C. Ambrosch-Draxl, P. Blaha, and K. Schwarz, *J. Phys.: Condensed Matter* **1**, 4491 (1989).
  - <sup>51</sup> K. Schwarz, C. Ambrosch-Draxl, and P. Blaha, *Phys. Rev. B* **42**, 2051 (1990).
  - <sup>52</sup> S. Lany, P. Blaha, J. Hamann, V. Ostheimer, H. Wolf, and T. Wichert, *Phys. Rev. B* **62**, R2259 (2000).
  - <sup>53</sup> S. J. Asadabadi, S. Cottenier, H. Akbarzadeh, R. Saki, and M. Rots, *Phys. Rev. B* **66**, 195103 (2002).
  - <sup>54</sup> K. Terakura, *Progr. Theor. Phys.* **46**, 1007 (1971).
  - <sup>55</sup> K. Terakura, *J. Phys. F: Met. Phys.* **7**, 1773 (1977).
  - <sup>56</sup> E. Daniel and J. Friedel, *J. Phys. Chem. Solids* **24**, 1601 (1963).